

longitude position as Jupiter rotated.

The auroral patch characteristic of rotating with Jupiter is expected because the injected electrons also rotate with Jupiter (within several per cent at ~ 12 Jupiter radii¹⁵). Although the auroral patch of interest here was the brightest observed during the joint observation campaign, such patches are common within HST images. Likewise, the occurrence of jovian electron injections is also common¹⁵. The other energetic electron injections revealed in the Galileo data (Figs 2 and 4) map to regions (Fig. 5) that also show measurable auroral emissions. However, those emissions do not appear patch-like and may have been active even in the absence of injections.

Studies of Earth's magnetosphere¹³ suggest two different ways that injected energetic particles can generate auroral emissions. (1) The particle energy distributions are modified during injection and become unstable to exchanges of energy with magnetospheric wave modes. The waves scatter particles so that some travel narrowly along the magnetic field lines until they encounter the atmosphere. (2) The injected particle cloud is a high-pressure region and so electric current flows along its boundary. This pressure-driven (diamagnetic) current diverges along the leading and trailing edges of the rotating cloud because the magnetic field strength changes with radial distance. Currents are driven along the magnetic field lines towards and away from the planet and can interact strongly with plasmas close to the planet. At Jupiter, that interaction would yield downward accelerated electrons, and atmospheric auroral emissions, at the trailing edge of the rotating plasma cloud. Although there is substantial uncertainty in the magnetic mapping, the position of the auroral patch does match best with either the trailing edge of the electron cloud (the second mechanism) or the centre of that portion of the cloud that contained the higher-energy electrons measured (the first mechanism).

For an aurora resulting from the scattering process, the maximum power density that the measured (>20 keV) electron cloud can provide to the aurora is $60 \pm 30 \text{ erg cm}^{-2} \text{ s}^{-1}$. Higher power densities are possible with the electric current generation mechanism. Models of interaction between electrons and Jupiter's atmosphere²², recalculated with the energy distribution shapes measured in Fig. 2, yield about $3 \text{ erg cm}^{-2} \text{ s}^{-1}$ for the electron input needed to explain the auroral emissions. Thus, measured electrons can supply the requisite energy with scattering efficiencies of only 3% to 10% of the maximum. Auroral optical emission spectra were not available for this event to estimate independently the electron energies involved. However, recent Galileo auroral observations measured the tangent altitude (above the 1-bar atmospheric pressure level) of peak auroral emissions at 245 ± 30 km, with some emissions extending to an altitude of 120 ± 40 km (ref. 23). Atmospheric penetration of electrons modelled for diffuse aurorae require the involvement of over 48 keV electrons to explain even the peak auroral emissions^{24,22}. □

Received 8 November 2001; accepted 1 February 2002.

1. Konradi, A. Proton events in the magnetosphere associated with magnetic bays. *J. Geophys. Res.* **72**, 3829–3841 (1967).
2. Arnoldy, R. L. & Chan, K. W. Particle substorms observed at the geostationary orbit. *J. Geophys. Res.* **74**, 5019–5028 (1969).
3. DeForest, S. E. & McIlwain, C. E. Plasma clouds in the magnetosphere. *J. Geophys. Res.* **76**, 3587–3611 (1971).
4. Mauk, B. H. & Meng, C.-I. in *Auroral Physics* (eds Meng, C.-I., Rycroft, M. J. & Frank, L. A.) 223–240 (Cambridge Univ. Press, Cambridge, 1991).
5. Li, X. *et al.* Simulation of dispersionless injections and drift echos of energetic electrons associated with substorms. *Geophys. Res. Lett.* **25**, 3763–3766 (1998).
6. Satoh, T., Connerney, J. E. P. & Baron, R. L. Emission source model of Jupiter's H₃⁺ aurorae: A generalized inverse analysis of images. *Icarus* **122**, 1–23 (1996).
7. Clarke, J. T. *et al.* Far-ultraviolet imaging of Jupiter's aurora and the Io "footprint". *Science* **274**, 404–409 (1996).
8. Ballester, G. E. *et al.* Time-resolved observations of Jupiter's far-ultraviolet aurora. *Science* **274**, 409–413 (1996).
9. Satoh, T. & Connerney, J. E. P. Jupiter's H₃⁺ emissions viewed in corrected jovimagnetic coordinates. *Icarus* **141**, 236–252 (1999).

10. Waite, J. H. *et al.* Multispectral observations of Jupiter's aurora. *Adv. Space Res.* **26**, 1453–1475 (2000).
11. Waite, J. H. *et al.* An auroral flare at Jupiter. *Nature* **410**, 787–789 (2001).
12. Meng, C.-I., Rycroft, M. J. & Frank, L. A. *Auroral Physics* (Cambridge Univ. Press, Cambridge, 1991).
13. Kivelson, M. G. & Russell, C. T. (eds) *Introduction to Space Physics* (Cambridge Univ. Press, Cambridge, 1995).
14. Mauk, B. H., Williams, D. J. & McEntire, R. W. Energy-time dispersed signatures of dynamic injections in Jupiter's inner magnetosphere. *Geophys. Res. Lett.* **24**, 2949–2953 (1997).
15. Mauk, B. H. *et al.* Storm-like dynamics of Jupiter's inner magnetosphere. *J. Geophys. Res.* **104**, 22759–22778 (1999).
16. McIlwain, C. E. in *Earth's Magnetospheric Processes* (ed. McCormac, B. M.) 268–279 (Reidel, Hingham, 1972).
17. Konradi, A., Semar, C. L. & Fritz, T. A. Substorm-injected protons and electrons and the injection boundary model. *J. Geophys. Res.* **80**, 543–552 (1975).
18. Mauk, B. H. & Meng, C.-I. Characterization of geostationary particle signatures based on the 'injection boundary model'. *J. Geophys. Res.* **88**, 3055–3071 (1983).
19. Khurana, K. K. Euler potential models of Jupiter's magnetospheric field. *J. Geophys. Res.* **102**, 11295–11306 (1997).
20. Connerney, J. E. P., Acuña, M. H. & Ness, N. F. Modeling the jovian current sheet and inner magnetosphere. *J. Geophys. Res.* **86**, 8370–8384 (1981).
21. Connerney, J. E. P. *et al.* New models of Jupiter's magnetic field constrained by the Io flux tube footprint. *J. Geophys. Res.* **103**, 11929–11939 (1998).
22. Grodent, D., Waite, J. H. Jr & Gérard, J.-C. A self-consistent model of the jovian auroral thermal structure. *J. Geophys. Res.* **106**, 12933–12952 (2001).
23. Vasavada, A. R. *et al.* Jupiter's visible aurora and Io footprint. *J. Geophys. Res.* **104**, 27133–27142 (1999).
24. Ajello, J. *et al.* Galileo orbiter ultraviolet observations of Jupiter aurora. *J. Geophys. Res.* **103**, 20125–20148 (1998).

Acknowledgements

We gratefully acknowledge help from and discussions with R. W. McEntire and T. Choo, and the support of the Space Telescope Institute.

Competing interests statement

The authors declare that they have no competing financial interests.

Correspondence and requests for materials should be addressed to B.H.M. (e-mail: Barry.Mauk@juapl.edu).

Bandgap modulation of carbon nanotubes by encapsulated metallofullerenes

Jhinwhan Lee*†, H. Kim*†, S.-J. Kahng‡, G. Kim*, Y.-W. Son*, J. Ihm*, H. Kato§, Z. W. Wang§, T. Okazaki§, H. Shinohara§ & Young Kuk*†

* School of Physics and † Center for Science in Nanometer Scale, Seoul National University, Seoul 151-747, Korea

‡ Department of Physics, Soongsil University, Seoul 156-743, Korea

§ Department of Chemistry, Nagoya University, Nagoya 464-8602, Japan

Motivated by the technical and economic difficulties in further miniaturizing silicon-based transistors with the present fabrication technologies, there is a strong effort to develop alternative electronic devices, based, for example, on single molecules^{1,2}. Recently, carbon nanotubes have been successfully used for nanometre-sized devices such as diodes^{3,4}, transistors^{5,6}, and random access memory cells⁷. Such nanotube devices are usually very long compared to silicon-based transistors. Here we report a method for dividing a semiconductor nanotube into multiple quantum dots with lengths of about 10 nm by inserting Gd@C₈₂ endohedral fullerenes. The spatial modulation of the nanotube electronic bandgap is observed with a low-temperature scanning tunnelling microscope. We find that a bandgap of ~ 0.5 eV is narrowed down to ~ 0.1 eV at sites where endohedral metallofullerenes are inserted. This change in bandgap can be explained by local elastic strain and charge transfer at metallofullerene sites. This technique for fabricating an array of quantum dots could be used for nano-electronics⁸ and nano-optoelectronics⁹.

Since the discovery of carbon nanotube a decade ago¹⁰, scientists have synthesized a variety of forms of carbon nanotubes. Recently, it has been shown experimentally that fullerenes or endohedral metallofullerenes¹¹ such as Gd encapsulated inside C₈₂ (Gd@C₈₂:GdMF) can be inserted into single-wall nanotubes (SWNTs), forming a pea-pod-like structure^{12–15}. When the diameter of the inserted fullerene is smaller than that of the SWNT minus a certain length (~0.7 nm, roughly twice the van der Waals bond length¹⁶), the fullerenes are inserted exothermally^{12,18}. When the diameter of a fullerene slightly exceeds the length described above, the fullerene can be inserted endothermally, but the resultant SWNT is elastically strained. A theoretical study has predicted that the electronic structure is severely modified, including the positions of the van Hove singularities (VHS), when an SWNT is uniaxially strained¹⁹. As we combine these ideas, we can perform ‘local bandgap engineering’ at the site where a fullerene is endothermally inserted. As schematically shown in Fig. 1a, we predict that the bandgap of a semiconducting nanotube would be altered by the insertion of large fullerenes.

The insertion of GdMFs into SWNTs was done by keeping them with SWNTs in a sealed glass ampoule at 500 °C for 3 days. The GdMFs were synthesized by a d.c. arc-discharge method^{11,12} and isolated with a multiple-step HPLC (high-performance liquid

chromatography) method¹⁵. The SWNTs were generated using a d.c. arc-discharging method with a graphite-metal composite rod and treated with acids to remove amorphous carbons. Previously reported TEM images and electron energy loss spectra^{14,15} suggested that the GdMFs can be spaced either regularly with 1.1 nm spacing or less regularly, with 1.1–3 nm spacing. The density of GdMFs could be controlled with sonication *ex situ* and/or annealing *in situ*. Figure 1b shows a typical STM image and the corresponding spatial variation of dI/dV along a SWNT without inserted fullerenes at a temperature of ~5 K. Scanning tunnelling microscopy and spectroscopy (dI/dV , where I is current and V is voltage) give bias-dependent topographic images and local density of states. To observe the local variation of the electronic structure, we took dI/dV spectra at 512 sites along the nanotube just after the topography was taken. The x axis indicates the position along the tube, the y axis the energy, and the colour scale dI/dV (shown at the right side of Fig. 1b). It takes 30–60 min to take 512 dI/dV spectra. Thermal drift is less than 0.1 nm h⁻¹ at this temperature. In the dI/dV spectra, two strong VHS peaks corresponding to the conduction and valence band edges are clearly visible with atomic resolution. As reported^{20,21}, the conduction and valence band edges are flat. When we imaged topographies of the SWNTs with inserted GdMFs (GdMF-SWNTs) at bias voltages of -0.8 V to +1.0 V, parts of the GdMF-SWNT appeared brighter than other areas, suggesting that the diameter may be greater there than at other areas or that the local electronic structure is modified by the inserted GdMFs as shown in Fig. 1c and d. Figure 1d shows a bundle of six GdMF-SWNTs, showing the variation of spacings between neighbouring GdMFs. We note that the density is still lower than the reported TEM results^{12,14}. About 10% of over 200 SWNT images showed locally bright spots in STM images.

Protrusions in STM topography do not necessarily indicate the exact locations of inserted GdMFs, because the electronic structures, including band edges, are severely modified with the insertion. Figure 2a shows spatial variation of dI/dV spectra along a GdMF-SWNT. The chirality of the GdMF-SWNT is determined to be (11,9) from the measured diameter of 1.4 nm (nominally 1.375 nm) and the chiral angle of 27° (nominally 26.7°). In the dI/dV spectra, conduction and valence band edges are also visible with two smaller VHS peaks following at higher bias voltages. The original bandgap of 0.43 eV is narrowed down to 0.17 eV at the sites where the GdMFs are expected to be located¹⁹. There are several causes which could account for the change in the bandgap:

(1) The magnetic field originating from the Gd atoms inside C₈₂ might cause this change. However, the magnetic flux of Gd (with the magnetic moment of ~8 μ_B) experienced by the SWNT is only ~10⁻⁵ flux quantum, so the effect of this phase variation on the

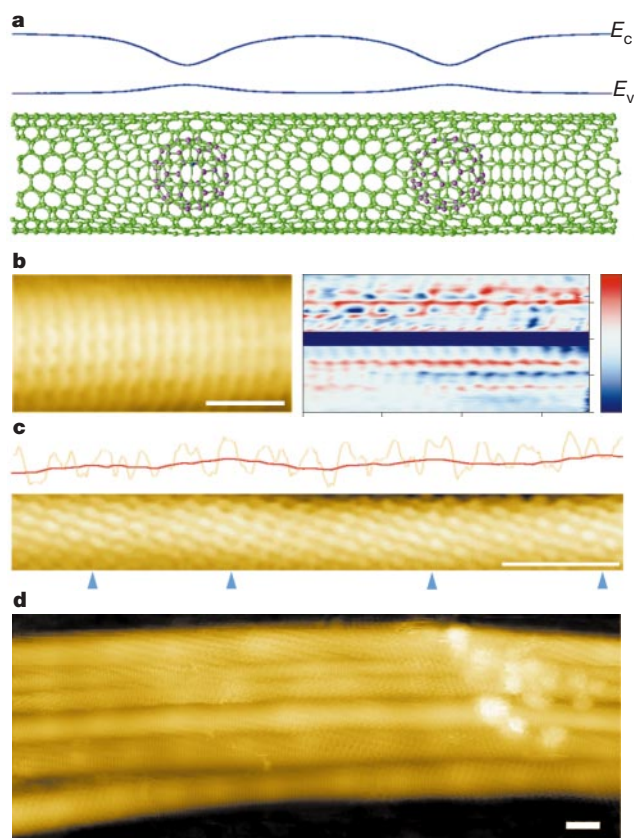


Figure 1 Effect of inserted Gd metallofullerenes (GdMFs) on the topography and band structure of a single-walled nanotube (SWNT). **a**, The illustration of a (11,9) GdMF-SWNT. Elastic strain is expected around the GdMFs. A schematic representation of estimated modulation of conduction (E_c) and valence (E_v) band edges is also shown. **b**, A typical topographic image of a SWNT obtained at the sample bias voltage of -0.3 V (left); the corresponding dI/dV spectra (right). The x axis represents the position along the SWNT, the y axis the energy in the range of -1.0 eV (bottom) to +0.87 eV (top), and the colour scale the local density of states. **c**, Atomically resolved topographic image of a (15,5) GdMF-SWNT at the sample bias voltages of 0.6 V. The GdMF sites are indicated by arrows. **d**, A bundle of six GdMF-SWNTs. Variation of spacings between neighbouring GdMFs are visible. The scale bars in all topographic images represent 1 nm.

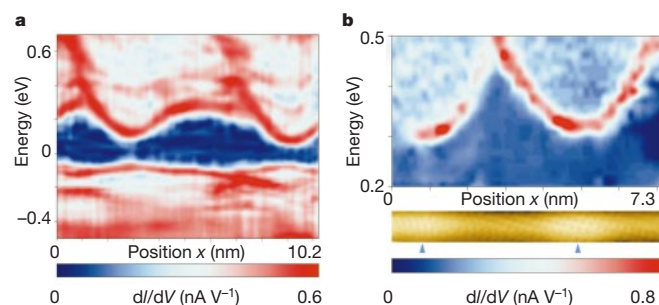


Figure 2 Bandgap modulation of a GdMF-SWNT by encapsulated GdMFs. **a**, The dI/dV spectra taken along the 10.2-nm-long GdMF-SWNT. The x axis represents the position along the GdMF-SWNT, the y axis the energy, and the colour scale the local density of states. **b**, Topographic image of a 7.3-nm-long (11,9) GdMF-SWNT at a sample bias voltage of 0.5 V. The sites of inserted GdMFs are indicated by arrows (bottom); the corresponding dI/dV spectra of conduction band at the centre of the GdMF-SWNT are also shown (top).

energy gap through the changed boundary condition around the SWNT is only 10^{-3} times the gap (<0.01 meV). Or, the energy shift of the electron on the SWNT by the magnetic field of Gd (~ 100 G) is again within 0.01 meV.

(2) The modulation of dI/dV along the GdMF-SWNT may possibly be due to the quantized electron-resonance states in a SWNT of short length or those localized between defects^{20,21}. However, bright spots appear even in a very long GdMF-SWNT and no correlation between the observed and expected results was found. We also observed the size effect of dI/dV spectra between two defects separated by ~ 5 nm in a plain SWNT²². The size effects resulted mainly in the intensity variation of VHS and the observed spatial variation of the local density of states is less than 0.1 eV.

(3) Charge transfer from the SWNT to the GdMFs or the Au(111) substrate may also induce a change in the electronic structure. The greatest effect of this mechanism is to shift the whole spectrum (both conduction and valence bands), together with some contribution to the energy-gap modification. Indeed, we notice that the Fermi level is closer to the valence band edge owing to the charge transfer, as though the SWNT were *p*-doped, and the majority of the modulation occurs in the conduction band.

(4) As suggested above, elastic strain can change the bandgap significantly. For example, a strain of 4% in the tube axis direction can induce a gap reduction of 60% for the (15,1) GdMF-SWNT¹⁹. To study the strain produced by fullerene insertion, we performed first-principles self-consistent pseudopotential calculations using the local density approximation. The Troullier–Martins nonlocal

pseudopotential in the separable Kleinman–Bylander form is employed with an energy cutoff of 40 Rydbergs (Ry). Localized basis orbitals are used to cope with a very large unit cell. The Gd atom is either not included or replaced by a simple metal (Mg) atom because of computational limitations. The results show the same trend as in ref. 19, but the maximum calculated strain in the relaxed geometry is $<1\%$ and the corresponding gap change is too small (<0.1 eV) compared with experiment.

We therefore conjecture that the combined contribution of the elastic strain and the electron transfer to the Au substrate and to C₈₂ may be responsible for the observed gap modulation. Unlike in the uniaxial strain, stretching in the circumferential direction is important here. One of the surprising features of these spectra is that the change in bandgap is so strongly localized that its spatial variation is clearly resolved in Fig 2a. At other locations along the GdMF-SWNT, we observed the modified conduction band of a different shape as shown in Fig. 2b. Various shapes of the modified energy band reflect the variation of local elastic strain and/or charge transfer or other physical quantities not listed here. The contributions of elastic strain and charge transfer to the change in bandgaps could be studied further by repeating the same experiments on SWNTs with plain fullerenes²³ and other types of metallofullerenes.

With the cylindrical symmetry of the SWNT alone, we would expect that its electronic structure might also show cylindrical symmetry. However, owing to the effect of the Au substrate, the cylindrical symmetry is reduced to at most a mirror-symmetry (with respect to the normal plane that cuts the SWNT in half along the tube axis). Mirror-symmetric distributions of the elastic strain and the charge transfer may occur. For example, the closer to the substrate, the greater is the charge transfer. That would give rise to the bending of the potential and shift of the VHSs with the above-mentioned mirror symmetry. When we took dI/dV images (a spatial map of the local electronic density of states²²) of a (15,5) GdMF-SWNT as a function of bias voltage, we found this expectation was correct. Figure 3a is a topographic image of a 7.6-nm-long GdMF-SWNT and Fig. 3b–j shows the corresponding dI/dV images at various bias voltages. The bandgap widening was observed at one site of this GdMF-SWNT in the tunnelling spectroscopy (not shown here). Mirror-symmetric, often sickle-shaped bright regions were observed here in Fig. 3b–j (indicated by arrows). The shift of the peaks in the local density of states marked by arrows in Fig. 3 is much greater than those of the two VHSs around the Fermi level in Fig. 2a. These peaks may be due to resonance tunnelling via unoccupied states associated with encapsulated GdMFs.

The present band structure represents one-dimensional multiple quantum dots, analogous to a multiple quantum well in a three-dimensional superlattice. The three-dimensional multi-layer utilizes the two-dimensionally confined carrier sub-bands for electronic and opto-electronic applications. The present multiple quantum dots may analogously be used for nano-optical devices. If the dots are periodic, the system can even be used for a quantum cascade laser⁹. With the bandgap modulation achieved here, we can create electron sub-bands in the potential-well regions. As we vary the density of the encapsulated fullerenes, the spacings between the quantum dots can be controlled. That would change the shape of the potential well for the electrons and holes. By inserting several different types of metallofullerenes, one-dimensional heterostructure, complex bandgap engineering can be achieved. With an additional electrode around the quantum wells, new one-dimensional electronic devices can be made. By using many identical quantum dots, this system could be applied to quantum computing⁸. We can also synthesize this bandgap-engineered system by self-assembly instead of by epitaxial growth. □

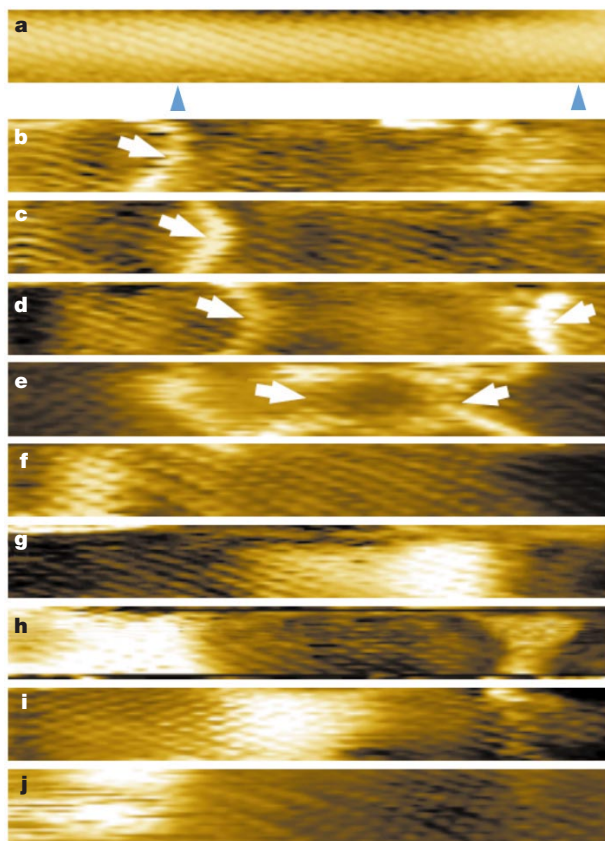


Figure 3 Energy-resolved dI/dV images of a GdMF-SWNT. The sites of inserted GdMFs are indicated by arrows. **a**, A topographic image of a 7.6-nm-long (15,5) GdMF-SWNT. **b–j**, The corresponding dI/dV images at the biases of **b**, 1.4; **c**, 1.2; **d**, 1.0; **e**, 0.8; **f**, 0.6; **g**, 0.4; **h**, 0.2; **i**, -0.2 ; **j**, -0.4 V. White arrows indicate that the position of the secondary-VHS shifts along the GdMF-SWNT by changing bias voltages, showing a large dispersion. Each bright line is sickle-shaped, which indicates that charge transfer or elastic strain varies around the GdMF-SWNT, breaking the cylindrical symmetry.

Received 15 August 2001; accepted 23 January 2002.

1. Aviram, A. & Ratner, M. (eds) *Molecular Electronics: Science and Technology*. (Annals of the New York Academy of Sciences, Vol. 852, New York, 1998).

2. Reed, M. A. & Tour, J. M. Computing with molecules. *Sci. Am.* **282**(6), 86–93 (June, 2000).
3. Yao, Z., Postma, H. W. Ch., Balents, L. & Dekker, C. Carbon nanotube intramolecular junctions. *Nature* **402**, 273–276 (1999).
4. Zhou, C., Kong, J., Yenilmez, E. & Dai, H. Modulated chemical doping of individual carbon nanotubes. *Science* **290**, 1552–1555 (2000).
5. Tan, S. J., Verschuere, A. R. M. & Dekker, C. Room-temperature transistor based on a single carbon nanotube. *Nature* **393**, 49–52 (1998).
6. Postma, H. W. Ch., Tijs, T., Yao, Z., Grifoni, M. & Dekker, C. Carbon nanotube single-electron transistors at room temperature. *Science* **293**, 76–79 (2001).
7. Rueckes, T. *et al.* Carbon nanotube-based nonvolatile random access memory for molecular computing. *Science* **289**, 94–97 (2000).
8. Toth, G. & Lent, C. S. Quantum computing with quantum-dot cellular automata. *Phys. Rev. A* **63**, 052315–052323 (2001).
9. Faist, J. *et al.* Continuous wave operation of a vertical transition quantum cascade laser above $T = 80$ K. *Appl. Phys. Lett.* **67**, 3057–3059 (1995).
10. Iijima, S. & Ichihashi, T. Single-shell carbon nanotubes of 1-nm diameter. *Nature* **363**, 603 (1993).
11. Shinohara, H. Endohedral metallofullerenes. *Rep. Prog. Phys.* **63**, 843–892 (2000).
12. Suenaga, K., Iijima, S., Kato, H. & Shinohara, H. Fine structure analysis of Gd M45 near-edge EELS on the valence state of Gd@C₆₀ microcrystals. *Phys. Rev. B* **62**, 1627–1630 (2000).
13. Smith, B. W., Monthieux, M. & Luzzi, D. E. Encapsulated C₆₀ in carbon nanotubes. *Nature* **396**, 323–324 (1998).
14. Suenaga, K. *et al.* Element-selective single atom imaging. *Science* **290**, 2280–2282 (2000).
15. Hirahara, K. *et al.* One-dimensional metallofullerenes crystal generated inside single-walled carbon nanotube. *Phys. Rev. Lett.* **85**, 5384–5387 (2000).
16. Smith, B. W., Luzzi, D. E. & Achiba, Y. Tumbling atoms and evidence for charge transfer in La₂@C₆₀/SWNT. *Chem. Phys. Lett.* **331**, 137–142 (2000).
17. Okada, S., Saito, S. & Oshiyama, A. Energetics and electronic structures of encapsulated C₆₀ in a carbon nanotube. *Phys. Rev. Lett.* **86**, 3835–3838 (2001).
18. Bandow, S. *et al.* Smallest limit of tube diameters for encasing of particular fullerenes determined by radial breathing mode Raman scattering. *Chem. Phys. Lett.* **347**, 23–28 (2001).
19. Yang, L. & Han, J. Electronic structure of deformed carbon nanotubes. *Phys. Rev. Lett.* **85**, 154–157 (2000).
20. Venema, L. C. *et al.* Imaging electron wave functions of quantized energy levels in carbon nanotubes. *Science* **283**, 52–55 (1999).
21. Lemay, S. G. *et al.* Two-dimensional imaging of electronic wavefunctions in carbon nanotubes. *Nature* **412**, 617–620 (2001).
22. Kim, H., Lee, J., Kahng, S.-J. & Kuk, Y. Spatial modulation of conduction and valence band edges around defects. *Phys. Rev. Lett.* (submitted).
23. Hornbaker, D. J., Kahng, S.-J., Misra, S. & Yazdani, A. Pseudo gaps and defect states in carbon nanotubes. *Proc. 11th Int. Conf. on Scanning Tunneling Microscopy/Spectroscopy Related Techniques* 104 (National Research Council, Vancouver, Canada, 2001).

Acknowledgements

We thank J.-Y. Park for his LTSTM design, Y. J. Song and H. S. Suh for experimental assistance, and J. J. Yu and S. W. Hwang for discussions. This work was supported by the Korean Ministry of Science and Technology through Creative Research Initiatives Program and the Future Program on New Carbon Nano-Materials by the Japan Society for the Promotion of Science.

Competing interests statement

The authors declare that they have no competing financial interests.

Correspondence and requests for materials should be addressed to Y.K. (e-mail: ykuk@phy.snu.ac.kr).

Factors determining crystal–liquid coexistence under shear

Scott Butler & Peter Harrowell

School of Chemistry, University of Sydney, Sydney, New South Wales 2006, Australia

The interaction between an imposed shear flow and an order–disorder transition underlies a broad range of phenomena. Under the influence of shear flow, a variety of soft matter^{1–4} is observed to spontaneously form bands characterized by different local order—for example, thermotropic liquid crystals subjected to shear flow exhibit rich phase behaviour⁵. The stability of order under the influence of shear flow is also fundamental to understanding frictional wear⁶ and lubrication^{7,8}. Although there exists

a well developed theoretical approach to the influence of shear flow on continuous transitions in fluid mixtures⁹, little is known about the underlying principles governing non-equilibrium coexistence between phases of different symmetry. Here we show, using non-equilibrium molecular dynamics simulations of a system of spherical particles, that a stationary coexistence exists between a strained crystal and the shearing liquid, and that this coexistence cannot be accounted for by invoking a non-equilibrium analogue of the chemical potential. Instead of such thermodynamic arguments^{10,11}, we argue that a balancing of the crystal growth rate with the rate of surface erosion by the shearing melt can account for the observed coexistence.

Our goal is to understand the nature of the coexistence between a crystal and its melt subjected to a shear flow. Specifically, we would like to test directly the proposition that non-equilibrium coexistence involves the balancing of properties of the bulk crystal and liquid phases (just as equilibrium coexistence involves balancing the crystal and liquid chemical potentials). In order to be able to calculate such bulk properties, we shall only consider states in which both bulk phases are responding linearly to the applied shear stress. This means that we shall not consider stresses in excess of the crystal yield stress—as occurs in the case of shearing colloidal crystals^{12–14}—nor, on the liquid side, will we consider phenomena such as shear-induced aggregation¹⁵ or hydrodynamic instabilities.

We report here the results of non-equilibrium molecular dynamics simulations of 2,592 Lennard–Jones particles sheared between two parallel walls, one amorphous and one crystalline. The normal to the (111) surface of the face centred cubic (f.c.c.) crystal lies parallel to the shear gradient, with the shear flow directed along the [110] direction. We find reproducible stationary states, corresponding to coexistence between the strained crystal and its shearing melt, for a range of temperatures T below the equilibrium melting point. An example of the calculated shear stress σ as a function of the applied shear rate $\dot{\gamma}$ is plotted in Fig. 1 along with the volume fraction f_l of the sample that is liquid. To determine f_l , we defined the dividing surface between crystal and liquid to be the point at which the structural order parameter X (as defined in Methods) equals 0.5. The shear stress is independent of the applied shear rate in the coexistence region, and a lever rule relates the fraction of crystal to liquid with the overall shear rate of the cell. (As required by mechanical stability, the shear stress is uniform throughout the two-phase system.) To avoid perturbations due to the walls, we have restricted our study to that part of the T – $\dot{\gamma}$ phase space for which the distance between the crystal–liquid interface

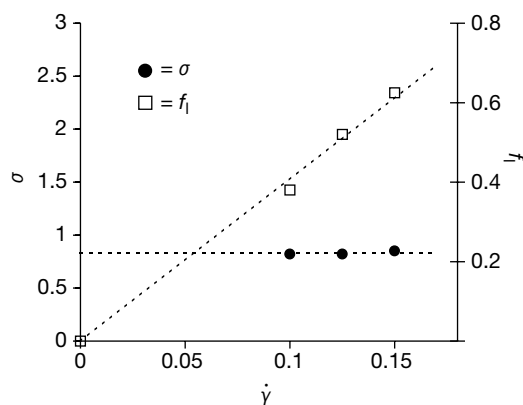


Figure 1 Shear stress σ and liquid volume fraction f_l versus the applied shear rate $\dot{\gamma}$ at $T = 0.7$. Note that σ is independent of $\dot{\gamma}$, whereas the liquid fraction is proportional to the applied shear rate. Although the applied shear rate $\dot{\gamma}$ is varied over the coexistence region, the actual shear rate of the liquid remains constant.